ACS NANO
Cite This: ACS Nano 2019, 13, 13910−13916
www.acsnano.org

ARTICLE

Stray-Field Imaging of a Chiral Artificial Spin Ice during Magnetization Reversal

Marcus Wyss,[†] Sebastian Gliga,[*,‡,¶] Denis Vasyukov,[†] Lorenzo Ceccarelli,[†] Giulio Romagnoli,[†] Jizhai Cui,[¶,§] Armin Kleibert,[¶] Robert L. Stamps,[∥] and Martino Poggio[†]

[†]Department of Physics, University of Basel, 4056 Basel, Switzerland
[‡]SUPA, School of Physics and Astronomy, University of Glasgow, Glasgow, G12 8QQ, United Kingdom
[¶]Paul Scherrer Institute, Villigen 5232, Switzerland
[§]Laboratory for Mesoscopic Systems, Department of Materials, ETH Zürich, 8093 Zürich, Switzerland
[∥]Department of Physics and Astronomy, University of Manitoba, Winnipeg, R3T 2N2, Canada

Supporting Information

ABSTRACT: **Artificial spin ices are a class of metamaterials consisting of magnetostatically coupled nanomagnets. Their interactions give rise to emergent behavior, which has the potential to be harnessed for the creation of functional materials. Consequently, the ability to map the stray field of such systems can be decisive for gaining an understanding of their properties. Here, we use a scanning nanometer-scale superconducting quantum interference device (SQUID) to image the magnetic stray field distribution of an artificial spin ice system exhibiting structural chirality as a function of applied magnetic fields at 4.2 K. The images reveal that the magnetostatic interaction gives rise to a measurable bending of the magnetization at the edges of the nanomagnets. Micromagnetic simulations predict that, owing to the structural chirality of the system, this edge bending is asymmetric in the presence of an external field and gives rise to a preferred direction for the reversal of the magnetization. This effect is not captured by models assuming a uniform magnetization. Our technique thus provides a promising means for understanding the collective response of artificial spin ices and their interactions.**

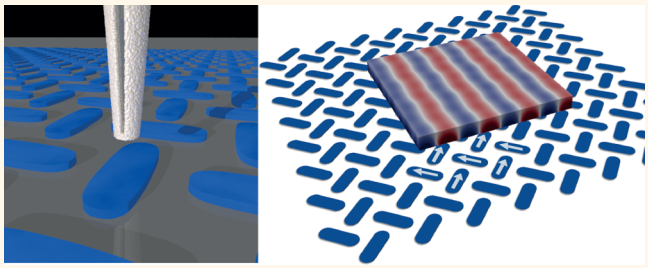

KEYWORDS: *artificial spin ice, scanning SQUID microscopy, nanomagnetism, magnetization reversal, chirality*

Artificial spin ices consist of geometrically arranged arrays of lithographically patterned interacting nanomagnets, whose shape anisotropy defines two possible orientations of the static magnetization in each nanomagnet.[1] While these systems were originally designed to mimic the frustration found in rare earth pyrochlore compounds,[2] it has recently become clear that their geometric arrangement can be tailored to create materials with topology by design, which exhibit rich collective dynamics.[3] For example, artificial spin ice can be tailored to support topological charge defects[2,4,5] whose dynamics can be controlled[6,7] and potentially exploited for applications such as energy storage.[8] It has also been demonstrated that artificial spin ices possess rich excitations in the GHz regime[9−12] and can be tailored to act as metamaterials for spin waves.[13,14] Moreover, specific geometries can be used to control magnetic ordering in the ground state[15] as well as during thermal excitation[16] and through external magnetic fields.[17,18] In particular, it was demonstrated that an artificial spin ice with a chiral geometry can be used to create an active material in which the collective rotation of the average magnetization proceeds in a single sense during thermal relaxation, thus exhibiting ratchet behavior.[19] These dynamics were attributed to the topology of the magnetostatic field generated at the edges of the lattice, highlighting the importance of understanding the stray field distribution in such systems.

While a number of imaging techniques have been used to measure the static,[20,21] quasi-static,[22−24] and dynamic[10,11] properties of artificial spin ices, none of these have mapped the stray field during magnetization dynamics. Here, we use a nanometer-scale scanning superconducting quantum interference device (SQUID) with sub-micrometer lateral resolution to quantitatively map the out-of-plane magnetic stray field $B_z(x, y)$ of an artificial spin ice system as it is led through magnetic reversal at 4.2 K.[25,26] This technique allows imaging stray field patterns in the presence of external magnetic fields up to $\mu_0 H_\perp = \pm 1.0$ T for out-of-plane fields and up to $\mu_0 H_\parallel =$

Received: July 10, 2019
Accepted: December 10, 2019
Published: December 10, 2019

DOI: 10.1021/acsnano.9b05428
ACS Nano 2019, 13, 13910−13916

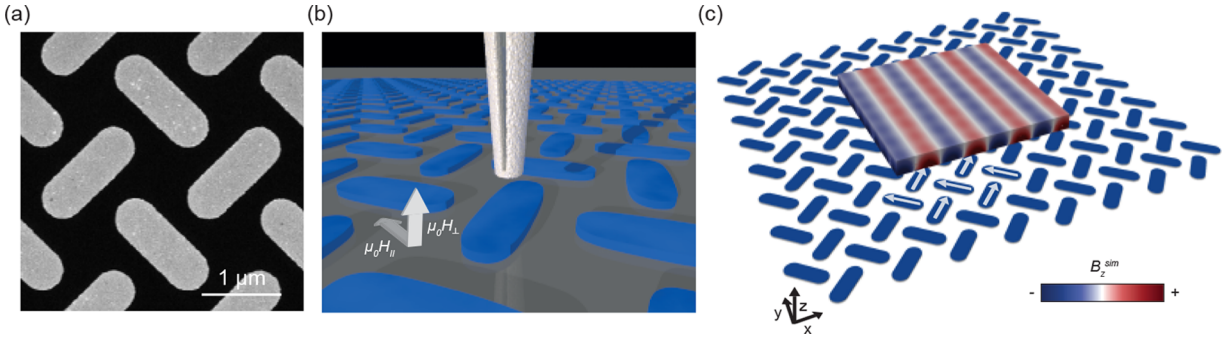

Figure 1. (a) Scanning electron microscopy (SEM) image of a vertex with chiral geometry. (b) Schematic drawing of the scanning nanoSQUID setup. By scanning the sample in the *xy*-plane, the *z*-component of the sample magnetic stray field $B_z(x, y)$ can be measured. (c) Simulated chiral ice array at remanence. The white arrows represent the average magnetization within a few nanomagnets. The stray field $B_z^{sim}(x, y)$ is calculated in a region ranging between 190 and 540 nm above a portion of the sample. The colormap indicates the field polarity.

±0.4 T for in-plane fields. The investigated artificial spin ice system is a "chiral" ice,[19] which consists of a periodic pattern of four-nanomagnet vertices exhibiting geometric chirality in two dimensions, shown in Figure 1a. In contrast to the experiments in ref 19, which have demonstrated dynamic chirality during thermal relaxation at room temperature, our system has substantially thicker, "frozen-in" nanomagnets (see Methods), and the magnetization dynamics are driven by an external field.

Figure 1b is a schematic representation of the scanning nanoSQUID setup. By scanning the sample in the *xy*-plane, the sample's magnetic stray field distribution $B_z(x, y)$ can be measured. A simulated example of the resulting stray field map of the chiral ice at remanence is shown in Figure 1c, and the evolution of the stray field pattern as a function of height is given in Supplementary Figure S1. Imaging the spatial configuration of the stray field, $B_z(x, y)$, as a function of external in-plane fields, we find that, owing to the thickness of the nanomagnets, the magnetostatic interaction leads to the bending of the magnetization at their edges. This bending becomes most pronounced at low applied fields, close to remanence, and can be experimentally detected using our nanoSQUID when the tip is in close proximity to the sample. Moreover, based on micromagnetic simulations, we find that, in the presence of an external in-plane field, edge bending leads to an asymmetric energy landscape in which the clockwise and counterclockwise net rotations of the magnetization at an individual vertex are energetically inequivalent, leading to different switching fields for the two configurations. This chiral behavior cannot be described by assuming a uniform magnetization of the nanomagnets, demonstrating the importance of considering the large number of degrees of freedom of the magnetization in modeling its behavior. Moreover, the origin of the predicted behavior is different from the previously observed edge-driven dynamic chirality in very thin, thermally active systems with similar geometry, in which the magnetization of each nanomagnet was uniform.

RESULTS

Starting from saturation, we investigate the stray field pattern of the chiral ice driven by an in-plane field. Figure 2a–h show a series of measured stray field distributions $B_z(x, y)$ for different applied in-plane field strengths ranging from $\mu_0 H_\parallel$ = 250 mT to $\mu_0 H_\parallel$ = −250 mT. The direction of the in-plane field is represented by a blue arrow in Figure 2a and has a small angle with respect to the *y*-axis. The observed stray field patterns result from the magnetic volume charge distribution within the nanomagnets and appear as diagonal regions of alternating field polarities (red and blue colors in Figure 2). Owing to the evolution of the magnetic state, these diagonal patterns evolve into vertical patterns parallel to the *y*-axis around zero field.

To interpret the measured stray field patterns, we perform micromagnetic simulations (see Methods). The simulated stray field distributions $B_z^{sim}(x, y)$ obtained for each applied field value $\mu_0 H_\parallel$ are shown in Figure 2i–p at the same location within the array. A quantitative match between the measured and simulated magnetic stray field distributions establishes a probe-to-sample distance of 450 nm. The simulated magnetization distribution within the nanomagnets is plotted in the insets. Simulations indicate that while the magnetization within the nanomagnets is uniform at 250 mT, as the field strength is reduced, it starts to exhibit a noticeable bending at the edges (Figure 2k–l), which is schematically highlighted by the large white arrows. For field values between +10 and −10 mT, the magnetization aligns along the easy-axis of the magnetic structures, due to shape anisotropy, while the edge bending is maximal, since the magnetization at the edges is more susceptible to the applied field. At $\mu_0 H_\parallel$ = −10 mT, the magnetization in individual nanomagnets starts to reverse.

Simulations show that the reversal is mediated by vortex nucleation and expulsion (on time scales of a few tens of nanoseconds), leading to a reproducible, nonperiodic, stray field pattern (shown in Figure 2n). In the experiment, we observe a reproducible pattern (Figure 2f and in Supplementary Figure S3e). The differences between the measured and simulated patterns are attributed to the presence of edge roughness and pinning in the sample as well as to the possibility that the reversal might instead proceed through domain wall formation and propagation.[27] At $\mu_0 H_\parallel$ = −50 mT (Figure 2g), $B_z(x, y)$ is similar to the pattern measured at +50 mT with an inverted polarity, as expected. The measured stray field distributions in the reverse direction along the hysteresis loop display similar behavior and are shown in Supplementary Figure S3a–g. Figure 2q shows a simulated hysteresis loop, plotted within the range −50 mT < $\mu_0 H_\parallel$ < 50 mT. Close to zero field, the edge bending increases until switching occurs around −10 mT. The region labeled "1" corresponds to the reversal of the first sublattice of the system (in which the nanomagnets are mostly parallel to the applied field), while the region labeled "2" corresponds to the reversal of the second sublattice (in which the nanomagnets are almost perpendicular to the applied field).

DOI: 10.1021/acsnano.9b05428
ACS Nano 2019, 13, 13910–13916

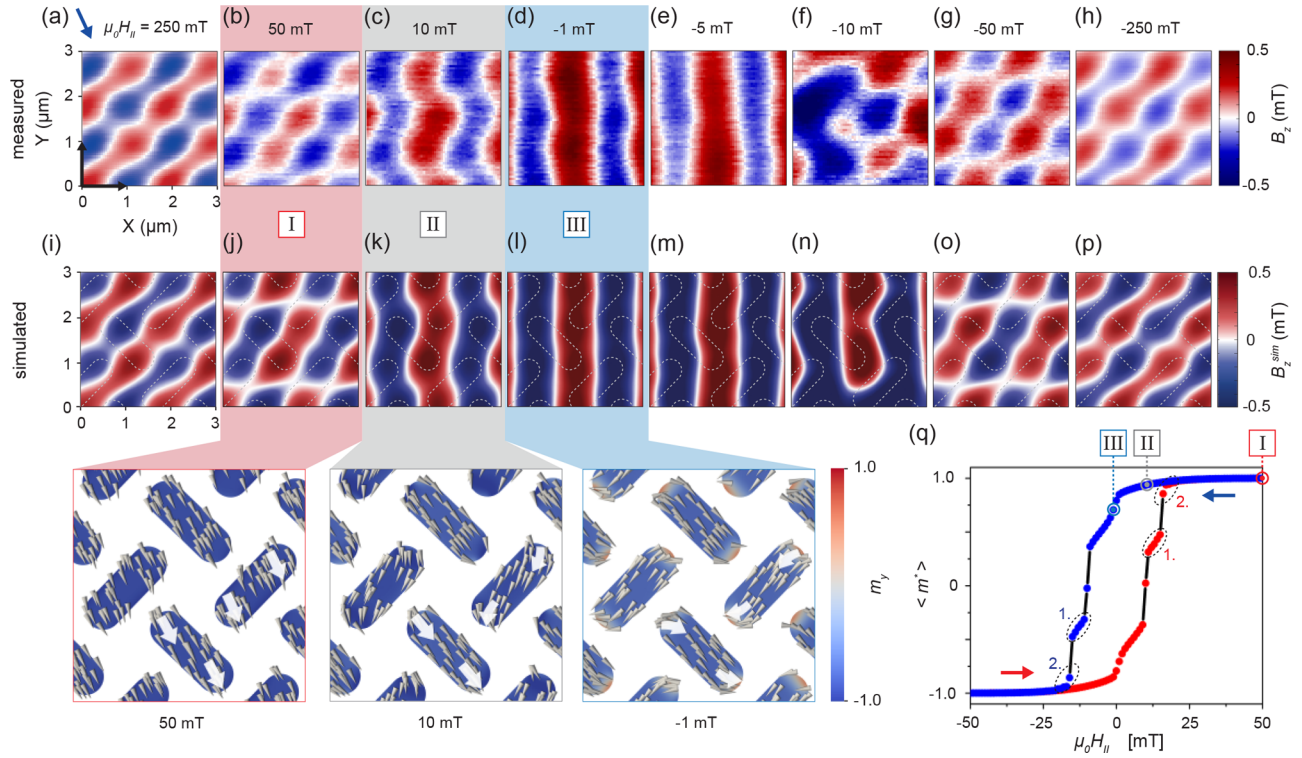

Figure 2. (a−h) Series of measured magnetic stray field distributions $B_z(x, y)$ for different values of the applied field, $\mu_0 H_{\parallel}$, whose direction is indicated in (a). (i−p) Corresponding series of simulated magnetic stray field distributions $B_z^{sim}(x, y)$, considering the same applied in-plane fields as in the experiment. The probe-to-sample distance is *ca.* 450 nm. The direction of $H_{\parallel}$ is shown by a blue arrow in (a). In (i)−(p) the dashed outlines indicate the positions of the nanomagnets. In the lower insets, the magnetization at a vertex is plotted using conical arrows. The direction of the magnetization at the edges of the nanomagnets is schematically highlighted by the thick white arrows and its bending is most clear at -1 mT. The colormap represents the *y*-component of the magnetization, m_y, where $m=M/M_s$. (q) Simulated hysteresis loop showing the two-step reversal of the nanomagnet lattice that occurs in the regions labeled "1" and "2". The quantity $\langle m^* \rangle$ is the component of the average magnetization along the field direction. The states labeled I−III correspond to the states shown in (j)−(l). The first reversal is preceded by states in which the magnetization displays increasing edge bending (state III for example), favoring the nucleation of vortices, which mediate the reversal.

While the simulations presented in Figure 2 indicate that the magnetization exhibits noticeable edge bending, it is not immediately clear to what extent the bending can be distinguished experimentally in the stray field maps. In the following, we establish that the effects of edge bending are measurable using our nanoSQUID upon reducing the tip-sample distance. In the top row of Figure 3, (a)−(c) show the measured stray field patterns for three different values of the external field along the same branch of the hysteresis loop as in Figure 2, for a reduced tip-to-sample height of 350 nm. Micromagnetic simulations of the equilibrium configurations (displaying edge bending) are shown in the second row of Figure 3, reproducing the measured stray field patterns. The third row shows the stray field distribution from simulations in which the magnetization of each nanomagnet is uniform. Differences in the simulated stray field distributions with and without edge bending become clear as the applied field is reduced and mostly drives the bending of the magnetization at the edges of the nanomagnets, leading to stray field patterns that increasingly differ from those of uniformly magnetized nanomagnets. Zoomed-in views of the stray field patterns at 5 mT in Figure 3c and f highlight the similarity between the measured data and the simulations in the presence of edge bending, in contrast to simulations with uniform magnetization, shown in Figure 3i.

The presence of edge bending in other artificial spin ice systems, such as the kagome[4] and square[2] ices, has been predicted to break vertex symmetry, modifying field-driven dynamics[28] and leading to the emergence of characteristic magnetic phases as well as to changes in the mode spectrum of the system.[29] Here, our simulations show that, in the presence of an applied in-plane field, edge bending has a direct impact on the energy of different magnetic configurations of the studied chiral ice, and consequently on the reversal paths of the magnetization. In Figure 4a, we consider a single vertex and compare the energy of the remanent state (labeled *RS*) with that of states in which the net vertex magnetization (represented by a green arrow) is rotated by 45° (labeled *CW45*, for the clockwise rotation and *CCW45* for the counterclockwise rotation) as well as by 90° (labeled *CW90* and *CCW90*) in the presence of a 2 mT field applied along the +*y* direction. The diagram in Figure 4b shows that the energy difference between the remanent state and states in which the net magnetization has rotated by 90° is approximately double of that between *RS* and states in which the magnetization has rotated by 45°. Moreover, *CW* and *CCW* states have energies that differ by a few eV in each case. In comparison, given that the experiments are performed at a temperature of 4 K, thermal excitation only amounts to $k_B T$ = 0.3 meV. Thus, the energy difference between the *CW* and *CCW* rotations is significant enough to give rise to chiral dynamics. We find, for

DOI: 10.1021/acsnano.9b05428
ACS Nano 2019, 13, 13910−13916

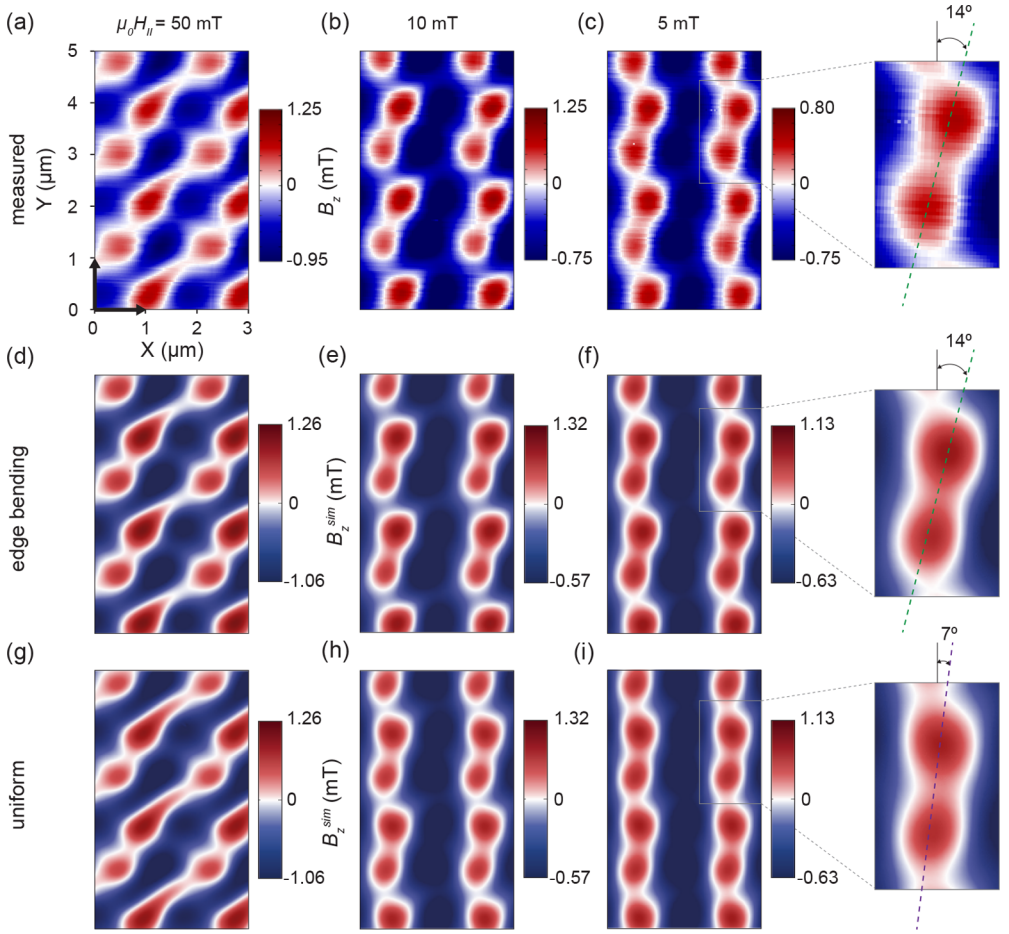

Figure 3. (a–c) Measured stray field maps $B_z(x, y)$ for different values of the applied external field, $\mu_0 H_{||}$. The probe-to-sample distance is reduced to 350 nm. (d–f) Simulated maps $B_z^{sim}(x, y)$ resulting from equilibrium configurations (for the same external field values) in which the magnetization displays edge bending. (g–i) Simulated $B_z^{sim}(x, y)$ distributions based on uniformly magnetized nanomagnets. The zoomed-in views of the patterns in (c), (f), and (i) highlight the orientation of the stray field patterns. Simulations in which the magnetization is uniform exhibit a different angle of the stray field pattern.

example, that fully reversing the magnetization of the vertex in the *CCW90* state requires a field of 9 mT, whereas reversing the magnetization of the *CW90* state requires 10 mT. (Reversing the magnetization of the *RS* state requires 11 mT.) Notably, although the simulations presented in Figure 4 are for a single vertex, we find that the results hold when considering *CCW* and *CCW* configurations of the net magnetization of a vertex within an array.

In contrast, considering nanomagnets with a uniform magnetization, we find that the *CW* and *CCW* energies are degenerate for both the 45° and 90° rotations (Figure 4c,d). These results demonstrate that the edge bending of the magnetization is responsible for the dynamic chirality: the direction of the edge magnetization induced by the external field differs in the *CW* and *CCW* states (see Figure 4a) owing to the broken symmetry of the system. Moreover, from Figure 4b and d, the configurations displaying edge bending have slightly lower energy differences with respect to *RS* than the configurations with uniform magnetization. While it is clear that edge bending minimizes the magnetostatic energy, this can also be understood in terms of the symmetries of the system: indeed, the magnetization in the vertices with uniformly-magnetized elements in *CW90* and *CCW90* states displays inversion symmetry. States displaying this fundamental symmetry generally have higher energies as compared to states in which it is broken,[30] such as for the *CW90* and *CCW90* states in the presence of edge bending. The rather modest asymmetry between the simulated energy differences considering uniform states and states exhibiting edge bending highlights the fact that even seemingly small perturbations can lead to measurable effects in the presence of symmetry breaking. We note that in the presence of a field whose direction is tilted with respect to the *y* axis, as in Figure 2, the reversal of the nanomagnets, which are most closely parallel to the field, is favored, leading to a similar, apparently chiral behavior, which is however not intrinsic. For example, assuming a 2 mT field applied at the same angle as in Figure 2, we find that the energy difference between the *CW90* and *CCW90* states is larger (*ca.* 50 eV) and, in contrast, favors the *CW* rotation, thereby overriding the chiral dynamics defined by edge bending.

The difference in energies and, consequently, in switching fields of different configurations in the presence of edge bending is expected to lead to favored magnetization reversal paths in larger systems. In a recent experimental study, Li *et al.*[17] have indeed observed that magnetization reversal in the chiral ice geometry is mediated by the formation of mesoscopic domains, separated by boundary regions defined by a limited number of vertex states with topologies resembling those of ferromagnetic domain walls. While these topologies were

DOI: 10.1021/acsnano.9b05428
ACS Nano 2019, 13, 13910–13916

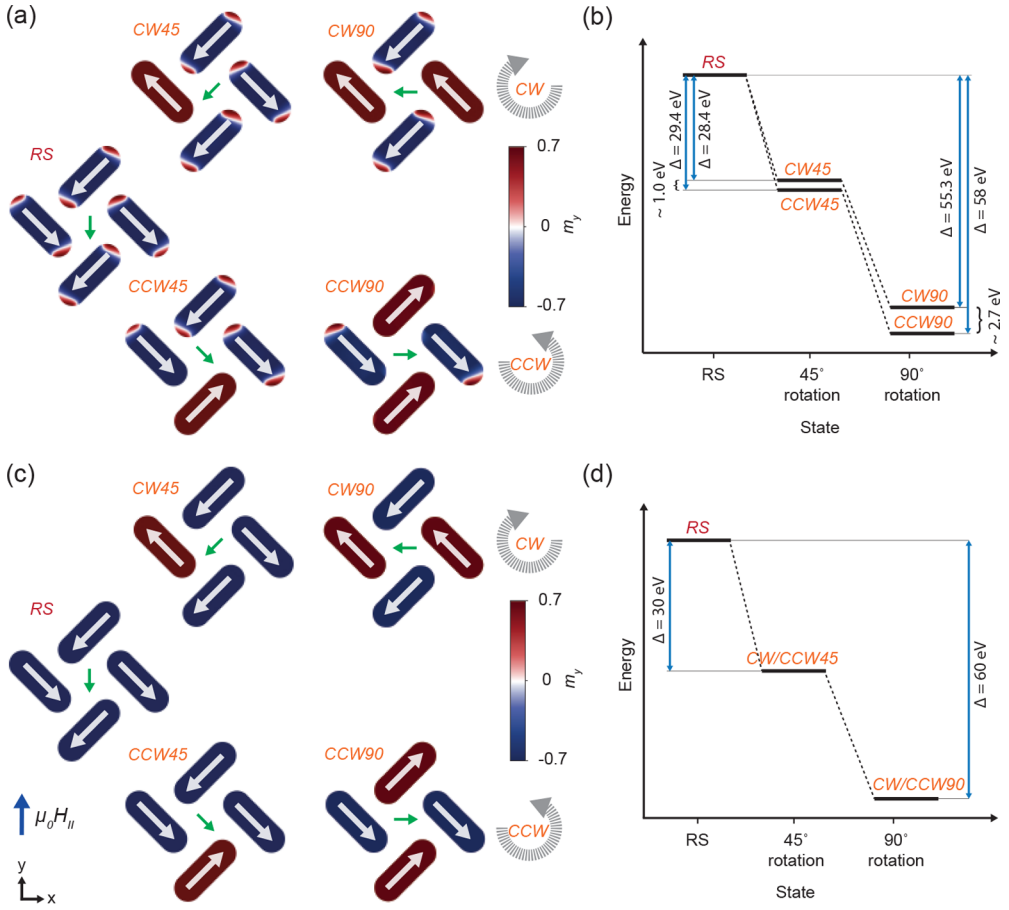

Figure 4. Simulated magnetization configurations and energies of a single vertex in the presence of a field $\mu_0 H_{||}$ = 2 mT, applied in the +*y* direction. In (a), the simulations include bending of the magnetization at the nanomagnet edges. The net vertex magnetization in each state is represented by a green arrow at the center of the vertex. In (b) the energy differences between *RS* and states in which the net vertex magnetization is rotated clockwise (*CW*) or counterclockwise (*CCW*) by 45° and 90° is schematically shown. In (c), the simulations assume a uniform magnetization in each nanomagnet, while (d) gives the energy differences for the same intermediate states.

found to be dependent on the angle of the applied reversal field, we expect these to additionally be influenced by the predicted intrinsic chirality of the system, in particular when the field angle is close to zero. Moreover, the chiral boundaries of arrays with a similar geometry have been shown to play a role in the magnetization reversal process[31] and may compete with the intrinsic chirality studied here, which occurs in the bulk of the array.

CONCLUSION

We have performed scanning SQUID-on-tip measurements of a spin ice system and measured the evolution of its stray field as a function of an applied external field. Our experiments, supported by micromagnetic simulations, demonstrate that the individual nanomagnets are not in a uniform state, but that their magnetization instead exhibits a strong bending at the edges of the nanostructures. Moreover, while the presence of edge bending has been studied in other artificial spin ice systems and was predicted to give rise to a characteristic magnetic phase as well as to changes in the mode spectrum of the system,[29] we predict that edge bending in the chiral ice geometry gives rise to an asymmetric energy landscape at individual vertices in the presence of an applied field. This favors the reversal of configurations in which the magnetization has rotated counterclockwise (with respect to the remanent state), giving rise to chiral dynamics. These results demonstrate how the presence of a large number of degrees of freedom of the magnetization can give rise to complex emergent behavior. Such behavior can be exploited to create artificial spin systems in which magnetic states could be tailored to design functional materials[32,33] such as super-ferromagnets[15,17] with tunable ground states and controllable reversal paths or reconfigurable[27] magnonic crystals[13,34] with topologically protected states.[14] These may enable future schemes for computing based on artificial spin ices.[35−37]

METHODS

Sample Preparation. Large 230 μm × 230 μm arrays consisting of Permalloy ($Ni_{83}Fe_{17}$) nanomagnet ensembles with chiral geometry as shown in Figure 1a were fabricated on a nonmagnetic Si(100) substrate using electron beam lithography combined with thermal evaporation at room temperature and a base pressure of 10^{-6} mbar followed by lift-off. The nanomagnets had a length and width of 1.55 μm and 560 nm, respectively, and a lattice constant of 1.5 μm (center-to-center distance of neighboring nanomagnets). To prevent oxidation, a 2 nm thick aluminum capping layer was evaporated on top of the Permalloy. Atomic force microscopy (AFM) was used to measure the thicknesses of the arrays, which was measured to be 10 nm on average across the entire array, without taking the capping layer into account. Each nanomagnet had a homogeneous surface, and the general shape displayed a high quality. Both are important factors to avoid a multidomain state, which is not desirable. The size of the nanomagnets was chosen such that essential features (such as the

DOI: 10.1021/acsnano.9b05428
ACS Nano 2019, 13, 13910−13916

separation between neighboring magnets as well as the spatial extent of the edge bending of the magnetization) were large enough to match the experimental resolution of the tip, while the thickness was chosen to ensure that the nanomagnets were in a single-domain state. The single-domain nature of the magnetic state was determined using X-ray photoemission electron microscopy (XPEEM).[38]

Measurements. SQUID-on-tips were pulled to achieve the required SQUID-on-tip (SOT) diameter and fabricated using a three-step evaporation of Pb on the apex of a quartz capillary according to the technique described by Vasyukov *et al.*[25] The Pb evaporation was performed in a custom-made evaporator with a rotatable sample holder cooled by liquid ^{4}He with a base pressure of 2×10^{-8} mbar. For protection of the SOTs against electrostatic discharge, a Au shunt was deposited close to the tip apex prior to the Pb evaporation. SOTs were characterized in a test setup prior to their use in the scanning probe microscope. The SOTs used here had effective diameters between 100 and 150 nm, as determined by measurements of the critical current as a function of a uniform magnetic field applied perpendicular to the SQUID loop. The sub-μm resolution is limited by the spacing and—ultimately—the SOT diameter. Measurements of the critical current show pronounced oscillations as a function of $H_\perp$ up to $\mu_0 H_\perp = \pm 1.0$ T and $\mu_0 H_\parallel = \pm 0.4$ T (see Supplementary Figure S1). We measured the magnetization evolution within the center of the arrays (*i.e.*, far from the edges) in response to an applied field. The angle of the field, indicated in Figure 2a, was due to the experimental setup. Additionally, for each in-plane field strength, a small out-of-plane magnetic field is applied, which ensures that the working point of the SOT is in the most sensitive region. This field is taken into account in the micromagnetic simulations and does not affect the magnetization within the nanomagnets due to their strong in-plane shape anisotropy (see Supporting Information).

Micromagnetic Simulations. Micromagnetic simulations[39] were performed by solving the Landau−Lifshitz−Gilbert (LLG) equation in three dimensions. The magnetostatic interaction, including the coupling between separate nanomagnets, is calculated using a hybrid finite-element/boundary element method. The simulations were carried out on a system of 144 nanomagnets, each with lateral dimensions of 833 nm × 290 and 10 nm thick. The simulated size corresponds to approximately 50% of the lateral size of the measured nanomagnets, keeping the thickness as in the experiments, in order to reproduce the bending of the magnetization at the nanomagnet edges. The structure was discretized using a tetrahedral mesh with an average cell size corresponding to an equivalent cube with a 5.7 nm side length. The simulated and measured stray field patterns were found to match for in-plane fields applied at an angle of 25° with respect to the *y*-axis. In Figure 4, the different states (*RS*, *CW*, *CCW*) were defined as initial configurations with uniform magnetization in each nanomagnet. The magnetization was dynamically relaxed into the lowest energy state in Figure 4a and b. The nanomagnets in the single vertex simulations have the same dimensions as in the array simulations. In Figure 2i−p, the magnetization was dynamically relaxed into the lowest energy state for the different field values, hence also capturing the dynamics during magnetization reversal. For the hysteresis loop (Figure 2q), the field was varied in increments of 0.5 mT between 250 and −250 mT, and the equilibrium states were obtained through energy minimization based on the conjugate gradient method. The simulations were performed with the following material parameters for Permalloy: saturation polarization $\mu_0 M_s = 1$ T, exchange constant $A_{ex} = 1.3 \times 10^{-11}$ J/m, and zero magnetocrystalline anisotropy $K = 0$, assuming a temperature of $T = 0$.

ASSOCIATED CONTENT

Supporting Information

The Supporting Information is available free of charge at https://pubs.acs.org/doi/10.1021/acsnano.9b05428.

Quantum interference pattern of the SQUID; simulated stray field patterns as a function of height with respect to the sample; in-plane field hysteresis loop (PDF)

AUTHOR INFORMATION

Corresponding Author

*E-mail: sebastian.gliga@psi.ch.

ORCID

Marcus Wyss: 0000-0001-9498-4108
Armin Kleibert: 0000-0003-3630-9360
Martino Poggio: 0000-0002-5327-051X

Notes

The authors declare no competing financial interest.

ACKNOWLEDGMENTS

We thank the machine shop of the Department of Physics at the University of Basel for assistance in the design of the measurement system. S.G. thanks V. Guzenko and E. Deckard for technical assistence as well as A. Kákay for discussions and technical help with the simulations. We acknowledge the support of the Kanton Aargau; the Swiss Nanoscience Institute; and the Swiss National Science Foundation through grant 200020-159893, grant 200020-178863, the Sinergia network Nanoskyrmionics (grant CRSII5-171003), and the NCCR Quantum Science and Technology (QSIT). S.G. has received funding by the European Union's Horizon 2020 research and innovation program under the Marie Skłodowska-Curie grant agreement no. 708674. J.C. has received funding from the European Union's Horizon 2020 research and innovation program under the Marie Skłodowska-Curie grant agreement no. 701647. R.L.S. acknowledges support from grant NSERC 05011-18. Use of the Center for Nanoscale Materials, an Office of Science user facility, was supported by the U.S. Department of Energy, Office of Science, Office of Basic Energy Sciences, under contract no. DE-AC02-06CH11357. Part of this work was performed at the Surface/Interface: Microscopy (SIM) beamline of the Swiss Light Source, Paul Scherrer Institute, Villigen, Switzerland.

REFERENCES

(1) Heyderman, L. J.; Stamps, R. L. Artificial Ferroic Systems: Novel Functionality from Structure, Interactions and Dynamics. *J. Phys.: Condens. Matter* **2013**, *25*, 363201.

(2) Wang, R. F.; Nisoli, C.; Freitas, R. S.; Li, J.; McConville, W.; J, C. B.; Lund, M. S.; Samarth, N.; Leighton, C.; Crespi, V. H.; Schiffer, P. Artificial 'Spin Ice' in a Geometrically Frustrated Lattice of Nanoscale Ferromagnetic Islands. *Nature* **2006**, *439*, 303.

(3) Nisoli, C. Topology by Design in Magnetic Nano-Materials: Artificial Spin Ice. In *The Role of Topology in Materials*; Gupta, S., Saxena, A., Eds.; Springer: Berlin, 2018; pp 85−112.

(4) Mengotti, E.; Heyderman, L. J.; Rodriguez, A. F.; Nolting, F.; Hugli, R. V.; Braun, H. B. Real Space Observation of Emergent Magnetic Monopoles and Associated Dirac Strings in Artifical Kagome Spin Ice. *Nat. Phys.* **2011**, *7*, 68.

(5) Farhan, A.; Saccone, M.; Petersen, C. F.; Dhuey, S.; Chopdekar, R. V.; Huang, Y.- L.; Kent, N.; Chen, Z.; Alava, M. J.; Lippert, T.; Scholl, A.; van Dijken, S. Emergent Magnetic Monopole Dynamics in Macroscopically Degenerate Artificial Spin Ice. *Sci. Adv.* **2019**, *5*, 2.

(6) Gilbert, I.; Chern, G.-W.; Zhang, S.; O'Brien, L.; Fore, B.; Nisoli, C.; Schiffer, P. Emergent Ice Rule and Magnetic Charge Screening from Vertex Frustration in Artificial Spin Ice. *Nat. Phys.* **2014**, *10*, 670−675.

(7) Farhan, A.; Scholl, A.; Petersen, C. F.; Anghinolfi, L.; Wuth, C.; Dhuey, S.; Chopdekar, R. V.; Mellado, P.; Alava, M. J.; van Dijken, S. Thermodynamics of Emergent Magnetic Charge Screening in Artificial Spin Ice. *Nat. Commun.* **2016**, *7*, 12635.

DOI: 10.1021/acsnano.9b05428
ACS Nano 2019, 13, 13910−13916

(8) Vedmedenko, E. Y. Dynamics of Bound Monopoles in Artificial Spin Ice: How to Store Energy in Dirac Strings. *Phys. Rev. Lett.* **2016**, *116*, 077202.
(9) Gliga, S.; Kákay, A.; Hertel, R.; Heinonen, O. G. Spectral Analysis of Topological Defects in an Artificial Spin-Ice Lattice. *Phys. Rev. Lett.* **2013**, *110*, 117205.
(10) Jungfleisch, M. B.; Zhang, W.; Iacocca, E.; Sklenar, J.; Ding, J.; Jiang, W.; Zhang, S.; Pearson, J. E.; Novosad, V.; Ketterson, J. B.; Heinonen, O.; Hoffmann, A. Dynamic Response of an Artificial Square Spin Ice. *Phys. Rev. B* **2016**, *93*, 100401.
(11) Li, Y.; Gubbiotti, G.; Casoli, F.; Gonçalves, F. J. T.; Morley, S. A.; Rosamond, M. C.; Linfield, E. H.; Marrows, C. H.; McVitie, S.; Stamps, R. L. Brillouin Light Scattering Study of Magnetic-Element Normal Modes in a Square Artificial Spin Ice Geometry. *J. Phys. D: Appl. Phys.* **2017**, *50*, 015003.
(12) Dion, T.; Arroo, D. M.; Yamanoi, K.; Kimura, T.; Gartside, J. C.; Cohen, L. F.; Kurebayashi, H.; Branford, W. R. Tunable Magnetization Dynamics in Artificial Spin Ice via Shape Anisotropy Modification. *Phys. Rev. B* **2019**, *100*, 054433.
(13) Iacocca, E.; Gliga, S.; Stamps, R. L.; Heinonen, O. Reconfigurable Wave Band Structure of an Artificial Square Ice. *Phys. Rev. B* **2016**, *93*, 134420.
(14) Iacocca, E.; Heinonen, O. Topologically Nontrivial Magnon Bands in Artificial Square Spin Ices with Dzyaloshinskii-Moriya Interaction. *Phys. Rev. Appl.* **2017**, *8*, 034015.
(15) Macêdo, R.; Macauley, G. M.; Nascimento, F. S.; Stamps, R. L. Apparent Ferromagnetism in the Pinwheel Artificial Spin Ice. *Phys. Rev. B* **2018**, *98*, 014437.
(16) Louis, D.; Lacour, D.; Hehn, M.; Lomakin, V.; Hauet, T.; Montaigne, F. A Tunable Magnetic Metamaterial Based on the Dipolar Four-State Potts Model. *Nat. Mater.* **2018**, *17*, 1076−1080.
(17) Li, Y.; Paterson, G. W.; Macauley, G. M.; Nascimento, F. S.; Ferguson, C.; Morley, S. A.; Rosamond, M. C.; Linfield, E. H.; MacLaren, D. A.; Macêdo, R.; Marrows, C. H.; McVitie, S.; Stamps, R. L. Superferromagnetism and Domain-Wall Topologies in Artificial "Pinwheel" Spin Ice. *ACS Nano* **2019**, *13*, 2213−2222.
(18) Jungfleisch, M. B.; Sklenar, J.; Ding, J.; Park, J.; Pearson, J. E.; Novosad, V.; Schiffer, P.; Hoffmann, A. High-Frequency Dynamics Modulated by Collective Magnetization Reversal in Artificial Spin Ice. *Phys. Rev. Appl.* **2017**, *8*, 064026.
(19) Gliga, S.; Hrkac, G.; Donnelly, C.; Büchi, J.; Kleibert, A.; Cui, J.; Farhan, A.; Kirk, E.; Chopdekar, R. V.; Masaki, Y.; Bingham, N. S.; Scholl, A.; Stamps, R. L.; Heyderman, L. J. Emergent Dynamic Chirality in a Thermally Driven Artificial Spin Ratchet. *Nat. Mater.* **2017**, *16*, 1106−1111.
(20) Morgan, J. P.; Stein, A.; Langridge, S.; Marrows, C. H. Thermal Ground-State Ordering and Elementary Excitations in Artificial Magnetic Square Ice. *Nat. Phys.* **2011**, *7*, 75−79.
(21) Phatak, C.; Petford-Long, A. K.; Heinonen, O.; Tanase, M.; De Graef, M. Nanoscale Structure of the Magnetic Induction at Monopole Defects in Artificial Spin-Ice Lattices. *Phys. Rev. B* **2011**, *83*, 174431.
(22) Farhan, A.; Derlet, P. M.; Kleibert, A.; Balan, A.; Chopdekar; Wyss; Perron, J.; Scholl, A.; Nolting, F.; Heyderman, L. J. Direct Observation of Thermal Relaxation in Artificial Spin Ice. *Phys. Rev. Lett.* **2013**, *111*, 057204.
(23) Zeissler, K.; Walton, S. K.; Ladak, S.; Read, D. E.; Tyliszczak, T.; Cohen, L. F.; Branford, W. R. The Non-Random Walk of Chiral Magnetic Charge Carriers in Artificial Spin Ice. *Sci. Rep.* **2013**, *3*, 1252.
(24) Zhang, S.; Gilbert, I.; Nisoli, C.; Chern, G.-W.; Erickson, M. J.; O'Brien, L.; Leighton, C.; Lammert, P. E.; Crespi, V. H.; Schiffer, P. Crystallites of Magnetic Charges in Artificial Spin Ice. *Nature* **2006**, *500*, 553−557.
(25) Vasyukov, D.; Anahory, Y.; Embon, L.; Halbertal, D.; Cuppens, J.; Neeman, L.; Finkler, A.; Segev, Y.; Myasoedov, Y.; Rappaport, M. L.; Huber, M. E.; Zeldov, E. A Scanning Superconducting Quantum Interference Device with Single Electron Spin Sensitivity. *Nat. Nanotechnol.* **2013**, *8*, 639−644.
(26) Vasyukov, D.; Ceccarelli, L.; Wyss, M.; Gross, B.; Schwarb, A.; Mehlin, A.; Rossi, N.; Tütüncüoglu, G.; Heimbach, F.; Zamani, R. R.; Kovács, A.; Fontcuberta i Morral, A.; Grundler, D.; Poggio, M. Imaging Stray Magnetic Field of Individual Ferromagnetic Nanotubes. *Nano Lett.* **2018**, *18*, 964−970.
(27) Gartside, J. C.; Arroo, D. M.; Burn, D. M.; Bemmer, V. L.; Moskalenko, A.; Cohen, L. F.; Branford, W. R. Realization of Ground State in Artificial Kagome Spin Ice *via* Topological Defect-Driven Magnetic Writing. Nat. *Nat. Nanotechnol.* **2018**, *13*, 53−58.
(28) Rougemaille, N.; Montaigne, F.; Canals, B.; Hehn, M.; Riahi, H.; Lacour, D.; Toussaint, J.-C. Chiral Nature of Magnetic Monopoles in Artificial Spin Ice. *New J. Phys.* **2013**, *15*, 035026.
(29) Gliga, S.; Kákay, A.; Heyderman, L. J.; Hertel, R.; Heinonen, O. G. Broken Vertex Symmetry and Finite Zero-Point Entropy in the Artificial Square Ice Ground State. *Phys. Rev. B: Condens. Matter Mater. Phys.* **2015**, *92*, 060413.
(30) Barpanda, P.; Kasama, T.; Dunin-Borkowski, R. E.; Scheinfein, M. R.; Arrott, A. S. Evolution and Propagation of Magnetic Vortices in Chains of Permalloy Nanospheres. *J. Appl. Phys.* **2006**, *99*, 08G103.
(31) Paterson, G. W.; Macauley, G. M.; Li, Y.; Macêdo, R.; Ferguson, C.; Morley, S. A.; Rosamond, M. C.; Linfield, E. H.; Marrows, C. H.; Stamps, R. L.; McVitie, S. Heisenberg Pseudo-Exchange and Emergent Anisotropies in Field-Driven Pinwheel Artificial Spin Ice. *Phys. Rev. B* **2019**, *100*, 174410.
(32) Lendinez, S.; Jungfleisch, M. B. Magnetization Dynamics in Artificial Spin Ice. *J. Phys.: Condens. Matter* **2020**, *32*, 013001.
(33) Skjærvø, S. H.; Marrows, C. H.; Stamps, R. L.; Heyderman, L. J. Advances in Artificial Spin Ice. *Nat. Rev. Phys.* **2019**, 2522−5820.
(34) Krawczyk, M.; Grundler, D. Review and Prospects of Magnonic Crystals and Devices with Reprogrammable Band Structure. *J. Phys.: Condens. Matter* **2014**, *26*, 123202.
(35) Arava, H.; Derlet, P. M.; Vijayakumar, J.; Cui, J.; Bingham, N. S.; Kleibert, A.; Heyderman, L. J. Computational Logic with Square Rings of Nanomagnets. *Nanotechnology* **2018**, *29*, 265205.
(36) Arava, H.; Leo, N.; Schildknecht, D.; Cui, J.; Vijayakumar, J.; Derlet, P. M.; Kleibert, A.; Heyderman, L. J. Engineering Relaxation Pathways in Building Blocks of Artificial Spin Ice for Computation. *Phys. Rev. Appl.* **2019**, *11*, 054086.
(37) Jensen, J. H.; Folven, E.; Tufte, G. Computation in Artificial Spin Ice. *2019 Conference on Artificial Life* **2018**, 15−22.
(38) Guyader, L. L.; Kleibert, A.; Rodriguez, A. F.; Moussaoui, S. E.; Balan, A.; Buzzi, M.; Raabe, J.; Nolting, F. Studying Nanomagnets and Magnetic Heterostructures with XRay PEEM at the Swiss Light Source. *J. Electron Spectrosc. Relat. Phenom.* **2012**, *185*, 371−380.
(39) Kákay, A.; Westphal, E.; Hertel, R. Speedup of FEM Micromagnetic Simulations with Graphical Processing Units. *IEEE Trans. Magn.* **2010**, *46*, 2303−2306.

DOI: 10.1021/acsnano.9b05428
ACS Nano 2019, 13, 13910−13916